Published in final edited form as:
Nature. 2018 April ; 556(7702): 483–486. doi:10.1038/s41586-018-0031-4.

Low loss Plasmon-assisted electro-optic modulator

Christian Haffner[1], **Daniel Chelladurai**[1], **Yuriy Fedoryshyn**[1], **Arne Josten**[1], **Benedikt Baeuerle**[1], **Wolfgang Heni**[1], **Tatsuhiko Watanabe**[1], **Tong Cui**[1], **Bojun Cheng**[1], **Soham Saha**[3], **Delwin L. Elder**[2], **Larry. R. Dalton**[2], **Alexandra Boltasseva**[3], **Vladimir Shalaev**[3], **Nathaniel Kinsey**[4], and **Juerg Leuthold**[1]

[1]ETH Zurich, Institute of Electromagnetic Fields (IEF), 8092 Zurich, Switzerland [2]University of Washington, Department of Chemistry, Seattle, WA 98195-1700, USA [3]Purdue University, School of Electrical & Computer Engineering and Brick Nanotechnology Center, West Lafayette, WIN 47909, USA [4]Virginia Commonwealth University, Department of Electrical and Computer Engineering, Richmond, VA 23284, USA

Abstract

For nearly two decades, the field of plasmonics1 - which studies the coupling of electromagnetic waves to the motion of free electrons in a metal2 - has sought to realize subwavelength optical devices for information technology3–6, sensing7,8, nonlinear optics9,10, optical nanotweezers11 and biomedical applications12. Although the heat generated by ohmic losses is desired for some applications (e.g. photo-thermal therapy), plasmonic devices for sensing and information technology have largely suffered from these losses inherent to metals13. This has led to a widespread stereotype that plasmonics is simply too lossy to be practical. Here, we demonstrate that these losses can be bypassed by employing “resonant switching”. In the proposed approach, light is only coupled to the lossy surface plasmon polaritons in the device’s off-state (in resonance) where attenuation is desired to ensure large extinction ratios and facilitate sub-ps switching. In the on state (out of resonance), light is prevented from coupling to the lossy plasmonic section by destructive interference. To validate the approach, we fabricated a plasmonic electro-optic ring modulator. The experiments confirm that low on-chip optical losses (2.5 dB), high-speed operation (>>100 GHz), good energy efficiency (12 fJ/bit), low thermal drift (4‰ K^{-1}), and a compact

---

Correspondence and requests for materials should be addressed to haffnerc@ethz.ch or leuthold@ethz.ch.

Author contributions:
C.H., N.K., V.S., A.B. and J.L. conceived the concept and supervised the project. C.H., D.C., S.S., and T.C. designed the modulator and developed the analytic frame work for fast optimization. T.W. designed the photonic grating coupler. C.H., D.C. and Y.F. fabricated the modulator and developed the required process technology. B.C. developed a focused ion beam process to image the cross section with minimal destructive influence on the suspended bridge. D.L.E., W.H., C.H., and L.R.D. developed, synthesized and implemented the poling procedure of the OEO-material for plasmonic ring resonators. C.H., and J.L., designed the experiments. C.H., D.C. and T.C. performed the passive characterization. C.H. performed the temperature sensitivity, DC switching and electro-optic bandwidth experiments. B.B., A.J. and C.H. performed the high-speed data experiment. B.B. and A.J. designed, calibrated, and automated the high-speed data experiment. B.B. and A.J. developed the digital-signal processing for data generation and analysis of the high speed data experiment. All authors discussed and analysed the data. C.H., N.K., D.C., and J.L. wrote the manuscript.

Author information:
Reprints and permissions information is available at www.nature.com/reprints.

No author has a competing financial interest.

footprint (sub-λ radius of 1 µm) can be realized within a single device. Our result illustrates the potential of plasmonics to render fast and compact on-chip sensing and communications technologies.

Telecommunication devices, such as electro-optic (EO) modulators must feature low insertion loss (IL) while providing a large phase (Δn) or amplitude ($\Delta \alpha$) change accumulated over a short device length14. Beyond that, modulators should offer low driving voltages and high-speed operation.

In recent years, silicon photonics has emerged which benefits from low propagation losses (dB/cm) but have struggled to achieve large modulation depth for sub-mm devices (Δn and $\Delta \alpha$)15. State-of-the-art devices maximize their modulation through the use of resonant structures16, enabling compact (μm^2-sized) and energy efficient components17,18. And while large Q-factors (on the order of a several 1000) enable a large reduction of the driving voltage, they limit the speed and increase the sensitivity of devices to temperature and fabrication fluctuations19. More recently, surface plasmonic polariton (SPP) devices have exploited the extreme confinement of light to achieve exceptional modulation within a few µm (Δn and $\Delta \alpha$)3,20. However, the metals that bring such promise to plasmonics are also the largest hindrance, as such devices suffer from large on-state loss (~dB/µm). To combat plasmonic losses, some devices employ hybrid-plasmonic-photonic modes4,6,21 while others minimize the length of the active section5,22. Still, typical IL of 10 dB due to the plasmonic propagation loss and photonic-to-plasmonic mode conversion loss remain a concern for high-speed state-of-the-art devices5,6. Thus, plasmonic on-chip technologies have been unable to replace the existing photonic or electronic solutions, placing the field of plasmonics at a crossroad to either abandon development or explore additional solutions.

We propose a novel approach, in which losses in plasmonic waveguides can be selectively used or bypassed to achieve low IL, strong modulation, compact footprint and high speed, simultaneously. This approach relaxes the prior goal to reduce the ohmic loss as much as possible to minimize the device’s on-state loss. Instead, we show that plasmonic losses can be tolerated by designing the device geometry such that light passes through the lossy section when required (in the off-state). To achieve this, we utilize a plasmonic ring resonator coupled to a buried low-loss silicon photonic waveguide, see Figure 1. Unlike prior approaches, which aim to reduce the resonator loss to realize high Q cavities or lasing7,23–26, our resonator exhibits typical propagation losses within the plasmonic cavity and mostly bypasses this lossy section in the on-state through destructive interference. Using this design, we demonstrate for the first time, a plasmonic modulator that is able to meet the key performance metrics of modern optical communications links.

Figure 1 shows the proposed device geometry, which comprises a gold metal-insulator-metal (MIM) slot waveguide ring coupled to a buried silicon bus waveguide, forming a notch filter with a resonant wavelength of (λ_{res}) (supplementary information: chapter II). The slot waveguide is filled with an organic electro-optic (OEO) material which alters the device’s resonance condition through the Pockels effect (Δn_{SPP})27. This enables a fast and selective use of the resonator’s Ohmic loss to attenuate the signal ($\Delta \alpha$) in the bus waveguide by applying a voltage.

Figure 1(c) shows the measured transmittance over the wavelength of two representative devices that differ in radius. For these structures, we have observed a distinct off-resonance ($\lambda_0 \neq \lambda_{res}$) and on-resonance ($\lambda_0 = \lambda_{res}$) condition at the telecommunication wavelength of 1.54 μm with an IL of 2.5 dB, an extinction ratio (ER) of 10 dB, and a Q-factor of ~30. Alternatively, we note that non-resonant devices based on MIM waveguides with a similar length feature an IL ranging from 8-10 dB5,6,22.

The reduced IL can be understood by comparing the exemplary operating principles of a non-resonant Mach-Zehnder (MZ)5, Figure 2 (I) and a resonant ring, Figure 2 (II). The IL of the device is a function of its coupling efficiency, geometry and accumulated ohmic loss. In both concepts, light couples to and from the plasmonic structure with a coupling efficiency (C). A transmission modulation is then induced by the Pockels effect over an active plasmonic section of length or circumference (l). The modulation depth (ΔT) – and also the loss (L_{SPP}) – scale with the length of the active plasmonic section6. Figure 2 shows the overall IL over the L_{SPP} in the active plasmonic area for a MZ and a critically coupled resonator. The arrows indicate the performance of devices with an equal ΔT.

The following points arise from Figure 2. First, the resonator's total loss is always smaller (blue curve < red curve) due to the bypassing mechanism28 . The IL increases with L_{SPP} (i.e. inverse to the cavity's Q-factor) as the critical coupling condition requires that more light couples to the plasmonic section. Second, the resonator has a 1 dB lower IL at $L_{SPP} \approx 0$ dB. This is because the non-resonant device requires two photonic-SPP converters as both the on- and the off-state propagate through the plasmonic section. Ohmic losses in the converters limit the conversion efficiency (C) to ~1 dB22,29. Contrarily, the selection mechanism of the resonator (on-state→bus waveguide; off-state→ ring) requires a converter which couples only a fraction of the light to the ring. Third, in the ring we take advantage of the resonantly enhanced ΔT to reduce the device length (supplementary information: chapter VII). For our resonant structures, we have calculated an enhancement of ~1.5. Consequently, our ring with a circumference of $l = 6$ μm ($L_{SPP} \approx 4$ dB) offers the same transmittance change as a MZ of $l = 9$ μm ($L_{SPP} \approx 6$ dB). In total, the ring device offers a 6 dB IL advantage over the MZ modulator. Additionally, losses can be further reduced by under-coupling the resonator as limited ERs of 10 dB are sufficient for many practical applications30.

To illustrate the modulation performance (ΔT) of the plasmonic resonator, the SPPs' effective refractive index (Δn_{SPP}) is altered by applying a bias between the inner and outer rings27. Figure 3 (a) shows the transmitted power versus applied voltage for a wavelength of ~1.52 μm. We observed an IL < 3 dB, an ER of ~10 dB, and a linear response (dashed green line) for a peak voltage of 3.5 V with an ER of ~6 dB. This performance in terms of IL and ER is similar to well-developed CMOS photonic resonators19. We estimate that operation under a digital driving voltage (1 V_{pp})19 is achievable in the near future by utilizing other plasmonic materials like silver or copper, using the newest OEO-materials and improving fabrication (methods: future improvements). To highlight the mechanism of the modulation the transmission of the device has been measured under a positive and negative bias of ±3.75 V as a function of wavelength, see Figure 3(b). This results in a normalized sensitivity ($S_\lambda / \Delta_{FWHM} = \Delta\lambda_{res}/(\Delta_{FWHM} \cdot \Delta n)$) of ~17 RIU^{-1}, assuming a relative change in OEO's refractive index of ~0.03. This can be compared to commercial SPR sensors that achieve values of 50 RIU^{-1} using a free-space Kretschmann configuration31. So, currently our approach is already close to the non-integrated free space approaches.

The moderate Q-factor guarantees a high operational speed and provides good thermal stability. For example, the measured resonance frequency is plotted in Figure 3(c) over a temperature range from 20°C up to 90°C. In this case, the resonant frequency is found to follow a linear trend line with a slope of ~0.4% K^{-1}. The insensitivity of the low-Q plasmonic resonator to temperature fluctuations is in strong contrast to high-Q photonic resonators, which are two orders of magnitude more sensitive to temperature fluctuations (~100% K^{-1})18. This is extremely beneficial for applications where strong temperature fluctuations occur. For example, a low-Q plasmonic resonant sensor or modulator would be immune to thermal fluctuations of ±5 °C which normally occur in CPUs while high-Q photonic resonators require power-consuming temperature controls to maintain operation19. Furthermore, the moderate Q factors are also beneficial for high-speed operation as desired in electro-optic modulators. As a result, we are able to push the bandwidth of a resonant electro-optic modulator well beyond 100 GHz (methods: speed limitations). In comparison, photonic resonators are more likely limited to bandwidths of ~20 GHz and below18,19.

Subsequently, we performed high-speed data experiments to demonstrate the robustness, high speed and low power switching capability. Although, the “resonant switching” principle can also be used to optimize sensors, we focus on high speed applications because their sensitivity and stability requirements are stricter.

In the experiment of Figure. 4(a) the peak driving voltage was ~3.3 V_{peak} and the laser wavelength was varied to capture the response of the modulator. Low device losses of 2.5 dB and fiber-to-silicon waveguide losses of ~7 dB resulted in fiber-to-fiber coupling losses of 16.5 dB enabling successful operation with low laser powers of 4 dBm and below. The resulting bit-error-ratio (BER) versus wavelength for a 72 Gbit/s signal is shown in Figure. 4(b) where a peak in the BER is observed at λ_{res}. A high BER is observed at λ_{res} since applying the same voltage with an opposing sign results in the same optical amplitude but a different phase. Consequently, we confirmed that the operating mechanism relies on amplitude modulation. Off-resonance, the BER quickly dropped to ~ 1×10^{-3} which is below the hard-decision forward error correction (HD-FEC) limit and allows for successful data modulation and detection32. No thermal heater was required for stabilization. Additionally, we reduced the data-rate to 36 Gbit/s and 18 Gbit/s and found BERs of ~ 2×10^{-6} and < 1×10^{-6}, respectively, indicating that the BER at 72 Gbit/s is mainly limited by the electrical equipment (methods: data experiments). We estimate the energy consumption of the modulator to be ~ 12 fJ/bit at 72 Gbit/s14 for a device capacitance of 1.1fF.

We demonstrate that low-Q resonant designs can enable low-loss active plasmonic devices with a good modulation depth by utilizing highly confined SPPs. We believe that our approach – unlike conventional resonant photonics – breaks the trade-off between sensitivity (high-Q) on the one hand and speed and temperature stability (low-Q) on the other. Our work can be seen as a step towards practical plasmonics that ultimately serves as a compact and fast gateway between electronics (local signal processing) and photonics (broad bandwidth and low-loss data stream). The proposed slot waveguide approach could be of interest in sensing because the resonant response can be exploited for many other material systems ranging from low index materials like aqueous solutions to high index materials such as silicon.

Methods

Future Improvements

The plasmonic material strongly influences the performance of the ring resonator in terms of losses and resonant enhancement. In this section, we discuss the influence of various plasmonic materials and we show that the modulator performance improves when replacing gold with copper (CMOS compatible) or silver (lowest loss).

In a first step, we investigate the unloaded Q-factor for different plasmonic metals. Extended Data Figure 1shows the unloaded quality factor Q as a function of the slot width and the radius for Au (a), Cu (b), and Ag (c).

Both copper and silver feature higher Q-factors. When changing the plasmonic metal from Au to Ag the quality factor is increased twofold for geometries dominated by propagation loss (Ag: 140/ Au: 60). Each material shows the trade-off between propagation loss and bending loss resulting in the characteristic triangular contour lines, see chapter III in supplementary information. Furthermore, using low loss materials such as silver will not only increase the intrinsic Q-factor, but also the coupling efficiency C. 3-D simulations indicate that C increases from 0.8 to 0.9.

Besides the plasmonic material, the OEO material provides an additional path for further improvement. Recent, experiments have shown that electro-optic (EO) coefficients over 300 pm/V are achievable by operating in close vicinity of the OEO material resonance ($\lambda \approx$ 1250 nm)33. Additionally, other OEO materials such as JRD134 show EO-coefficients >300 pm/V JRD135,36.

To evaluate the influence of these improvements on the modulator performance, Extended Data Figure 1 shows the wavelength-dependent transmittance of a MIM ring resonator obtained by the analytic model (equation (2) in supplementary information). Extended Data Figure 1(d) shows the transmittance for gold while Extended Data Figure 1(e) includes the possible improvements with Ag and JRD1 (EO coefficient of 300 pm/V). The radius is 1 μm, the slot width is 80 nm and the outer electrode height is 350 nm. The solid lines correspond to positive (blue) and negative (red) biasing of 2 V.

Such improved configurations offer through port IL as small as 0.5 dB (Ag) compared to 1.5 dB (Au). Furthermore, the switching sensitivity is significantly increased due to the higher nonlinearity (3 x) and the larger Q-factor (2 x). Thus, the absolute IL reduce form 4.3 dB to 1.2 dB and the ER increases from 2 dB to 18 dB when driven with ±2 V at the chosen probing wavelength (vertical green line). Thus, low-power CMOS transistors may drive the plasmonic resonators without the help of electrical amplification. This would reduce the total energy consumption of the modulators to below 1 fJ/Bit.

Alternative Active Materials for Modulation and Sensing

Here, we discuss the influence of the refractive index of the slot material on the unloaded Q-factor of plasmonic ring resonators. The active material could be either an OEO material for modulation or a bio-sensitive material for sensing purposes. Extended Data Figure 2 shows the simulated Q-factors for different slot widths and radii. The simulated refractive indices range from 1.33 up to 3.48 as shown in subplots (a) to (h).

All material systems achieve Q-factors above 30. The refractive index of the active material strongly influences the bending and propagation losses. In the case of low n_{slot}, for (a) and (b), the *Q*-factor is mainly limited by bending losses for all slot widths as indicated by the diagonal contour lines (dashed lines). This behaviour changes when n_{slot} increases to 1.75 (c) or 2 (d) and typical triangular contour lines can be observed highlighting the trade-off between bending losses and propagation losses, see section IV in supplementary information. A further increase of the refractive index results in dominating propagation losses. The triangular shape of the contour line changes to contour lines parallel to the R-axis. In this region, see subplot (e) to (h), the Q-factor drops for the same geometrical parameters as propagation loss increases with the refractive index37.

Subplots (a), (c),(e) and (h) are of most interest as they represent materials that can be used for sensing: (a) n_{slot} =1.33(H2O); or for EO-modulation: (c) n_{slot} =1.75 (OEO)35; (e) n_{slot} =2.25 (BTO)38; (h) n_{slot} =3.48(Si)22.

Sample Fabrication

All reported devices were processed on SOI wafers with a 220 nm thick silicon device layer and 3 µm thick buried oxide. Electron beam lithography (Vistec EBPG5200) in combination with ICP-RIE (Oxford Plasmalab System 100) were applied to pattern the silicon photonic components. A positive tone resist (PMMA) and a negative tone resist (HSQ) were used as masks to define the partially (70 nm) and fully (220 nm) etched silicon structures, respectively39. Planarization of the patterned silicon structures was realized by spin-coating the samples with a 1 µm thick HSQ layer followed by rapid thermal annealing to convert HSQ to $SiO_2$40. We observed thickness variations of ±10 nm with a periodicity of 50 µm throughout the chip. This does not affect device performance due to the large discrepancy in size between the footprint of the resonators and the periodicity. We controlled the coupling between the ring and bus waveguide by using the following protocol, which enabled us to adjust the average vertical spacing ($d_{\text{Au,Si}}$) within 5nm of the target value. First, we use an e-beam patterned PMMA resist mask to open Silicon etch marks placed next to the device to measure the HSQ thickness during the following wet etching process. Afterwards, we used a 2nd e-beam patterned PMMA resist to locally etch down the SiO_2 over the bus waveguide to the desired spacing $d_{\text{Au,Si}} = 70 \pm 10$ nm by using a buffered HF (7:1) solution. The slow etch-rate of 1.2 nm/s enables good process control. Please note, that the spin-coating process rather than the wet etching process introduce the uncertainty of ±10 nm. Contact pads, outer rings (h = 350 nm), inner rings (h = 150 nm) and bridges (h = 350 nm) were produced with a sequence of e-beam lithography, electron-beam evaporation of gold and lift-off processes as reported in Ref. 5. Extended Data Figure 3 shows a tilted top view of the fabricated ring resonator prior to the bridge fabrication step. The height of the outer electrode is 350 nm, while the inner electrode is only 150 nm enabling a reduction of the bending losses, see chapter IV in supplementary information.

Afterwards, we characterized the geometry of all devices using scanning-electron microscopy (SEM) for better comparisons to simulations. This, allows us to estimate important parameters such as the electro-optic coefficient, r_{33}, later on. Finally, the binary OEO material (75%HD-BB-OH/25%YLD124)41 was spin-coated then poled at its glass transition temperature (115 °C) by applying electric fields of ~130 V/μm. It has been shown that this OEO material allows operation up to 80 °C33.

We choose the following design parameter sets: slot widths of 80 nm and 100 nm with radii ranging from 900 nm to 1200 m and 1400 nm to 1600 nm.

Passive Characterization

We determined the transmittance of the resonators by subtracting back-to-back measurements of structures that comprise the same grating couplers and photonic waveguides but lack the plasmonic section. The standard deviation of the back-to-back measurements was below ±0.5 dB over the whole wavelength range of the tunable laser (1465 nm to 1635 nm). We measured the passive spectrum for various input power up to 10 dBm and didn't observe a drift of the resonance wavelength due to self-heating. To prevent any self-heating, we set the laser power to 0 dBm for the passive characterization.

Extended Data Figure 4 shows two histograms of the measured insertion loss (a) and extinction ratio (b) of 23 ring resonators with targeted slot widths of 80 nm. The average insertion loss is ~2.5 dB and the mean extinction ratio is ~9.7 dB.

We designed rings with varying radii to account for fabrication variations. Extended Data Figure 4(c) shows the passive spectrum of ring resonators with radii ranging from 940 nm up to 990 nm. The resonance wavelength shifts with increasing radius by $(\delta\lambda_{\mathrm{res}}/\delta R \approx 1.1)$

Sensitivity Experiments

We used the same optical setup as the passive characterization measurements to estimate the DC/ low frequency electro-optic response of six devices. In a first experiment, we applied a 100 Hz triangular shaped electrical signal with an amplitude of 10 V_{peak}. We measured the modulation of the optical signal when operating the resonator around its 3 dB point. In a second experiment, we applied a DC-bias and measured the resonators' wavelength shift as a function of the voltage. Extended Data Table 1 provides an overview of the insertion loss, extinction ratio and sensitivity of the resonance wavelength ($\Delta\lambda_{\mathrm{res}}$/V) as extracted from these two experiments. The *ER* (6-10 dB) and *IL* (2-3 dB) during active switching match the values obtained from passive characterization. This shows that the modulators can be driven from minimum to maximum output power before dielectric breakdown occurs. 3D simulation of device 79 revealed an $\Delta\lambda_{\mathrm{res}}/\mathrm{V} \approx 3.1\mathrm{nm/V}$ for an electro-optic coefficient of 100 pm/V. Thus, we estimate an in-device electro-optic coefficient of ~90 pm/V and a $\Delta n \approx 0.03$ when biasing with ±3.75 V based on the Pockels effect. Device 79 (last row) is shown in the manuscript Fig. 3(a) and (b).

Speed Limitations

The electro-optic bandwidth of resonant EO modulators is often determined by the photon lifetime of the resonant cavity. In case of a ring-based EO modulator with a Q-factor of 6000, this calculates to an electro-optic bandwidth of a few tens of GHz42. In the case of resonant plasmonic structures, the photon lifetime does not limit the electro-optic bandwidth since these structures feature Q-factors that are two orders of magnitude smaller than the Q-factors of photonic approaches.

In general, the slowest of the following effects limits the electro-optic bandwidth of an EO-modulator: 1) RC-time constant; 2) timescale of the nonlinear effect (here Pockels effect); and 3) cavity lifetime. In the case of the plasmonic MIM ring modulator presented in this work these contributions can be approximated to:

- **τ_{RC}:** The calculated capacitance of the MIM ring is ~1.1fF (electro-static 3D simulation), while its resistance is a few Ω with the nm-scaled bridge being the main contributor5. This results in a RC-bandwidth of **>>1 THz**.
- **$\tau_{Pockels}$:** The Pockels effect is based on the reorganization of π-electrons within a nm-long molecule and is estimated to be on the time scale of femto- or attoseconds27. This results in a Pockels-bandwidth of **>>1 THz**.
- **τ_{cavity}:** The SPP lifetime is given by the quality factor divided by the angular frequency ($\tau_{res} \approx Q/\omega_{photon}$). The resonant structures presented in this work feature Q-factors of 50, while future implementations may reach values of up to 150. Thus, the cavity lifetime of SPPs is ~100 fs or less, resulting in a cavity lifetime bandwidth limit of **> 1 THz**.

Based on these approximations, we expect, at worst, a THz bandwidth for a plasmonic MIM resonator utilizing the Pockels effect. To confirm that bandwidth limitations are not an issue for resonant plasmonic modulators we performed electro-optic bandwidth measurements with a plasmonic resonator of radius 1.5 μm and a designed slot width of 100 nm. These design parameters are chosen because they feature largest Q-factors and therefore the longest cavity lifetimes. Extended Data Figure 5(a) shows the wavelength dependent transmittance of the plasmonic resonators and (b) shows the normalized modulation efficiency as a function of the modulation frequency. The ratio between the unmodulated carrier and the modulated sidebands is the modulation efficiency which was measured with an optical spectrum analyzer and normalized with respect to the lowest applied frequency43.

The different colors correspond to three characteristic probing wavelengths. Red, yellow and purple are the off-resonance, 3 dB point and on-resonance probing wavelengths, respectively. For all three curves a similar behavior is observed and electro-optic bandwidths beyond 100 GHz are found. This indicates that the cavity lifetime is not yet limiting the bandwidth. Otherwise, a discrepancy in bandwidth between on-resonance (purple) and off-resonance (red) operation should be observed. The kink at ~110 GHz is attributed to limitations in the electrical test setup.

Two different measurement setups were required to cover the broad electrical spectrum ranging from 20 GHz up to 115 GHz in steps of 2.5 GHz. The 1st setup (20 GHz up to 70

GHz) utilized a tunable RF signal generator (100 kHz – 70 GHz) to generate a sinusoidal RF signal. The electrical output power of the source was adjusted for each frequency such that a constant power of 0 dBm was applied to the ring resonator via GSG probes. The 2nd setup was used to cover the frequency range from 70 GHz up to 115 GHz with a step size of 2.5 GHz. We used the 6th harmonic of a Schottky diode to generate these frequencies. The electrical input power to the Schottky diode was kept constant. We compensated the variations in the diode's output power by measuring the power with a broadband power meter. The measured power values were used in a post-processing step to subtract the influence of the varying power. The power levels of the harmonic terms other than the 6th harmonic were negligible.

Please note, the signal was applied via and 100 µm x 100 µm sized contact pads The resonator itself (~1.1fF) does not determine the total capacitance as the large contact pads interact with the substrate resulting in a capacitance of several 10s of fF44. The modulator behaves like an open circuit element due to the small capacitance.

Data Experiments

This section provides details about the experimental setup shown in Fig. 4 of the manuscript. A tunable, external cavity laser (1465 nm to 1575 nm) was used as a light source with output powers ranging from 6 dBm up to 13 dBm. The laser light was fed to an attenuator to enable a flexible adjustment of the optical power. Light was coupled to and from the chip via grating couplers, which have an efficiency (C_{GC}) of -7 dB each at 1550 nm. All non-return-to-zero (NRZ) electrical data streams were random binary sequences of length 218 generated by a 72 GSa/s, 6-bit digital to analog converter ($f_{3dB} \approx 20$ GHz). Afterwards, an RF amplifier ($f_{3dB} \approx 50\text{-}55$ GHz) amplified the electrical signal to a certain peak-to-peak driving voltage ($V_{pp,50\Omega}$ measured over a 50 Ω resistor. Finally, the electrical signal was applied by GS RF-probes ($f_{3dB} > 67$ GHz) to the device via 100 µm x 100 µm sized contact pads. Two 25 cm-long RF-cables (1.85 mm connectors) connected the generator, amplifier and RF probe. The modulated light was detected coherently. We used a second laser for heterodyne detection. The 3dB bandwidth of the coherent detector's photodiode is 70 GHz. An EDFA (Erbium Doped Fiber Amplifier) amplified the optical signal after the modulator to power levels of ~ 8 dBm to enable best performance. The electrical oscilloscope (Electrical bandwidth: 63 GHz and sampling rate: 160 GSa/s) sampled and digitized the waveform. Offline digital-signal-processing was performed to account for timing errors45, carrier frequency and phase offsets and the linear frequency response of the system by feedforward equalization with adaptive least mean square (LMS)-based filter updates. Extended Data Table 2 shows the results in terms of bit-error-ratio (BER) obtained from six different devices under various driving voltages (V_{peak}), data rates (R), and optical input powers at the grating coupler. Similar BERs are obtained for different devices under equal conditions. For instance, low BERs are obtained at 18 Gbit/s for small driving voltages of ~3.3 V_{peak} and low input powers. At 72Gbit/s the BER drops to 10^{-3} under similar conditions. We increased the driving voltages twofold and the input power fourfold and measured only a moderate reduction of the BER to 10^{-4}. We attribute this due to the limited bandwidth of the electrical components. Device 34 is shown in the manuscript Fig. 4.

Comparison State-of-the-Art EO Modulators

In the following we compare the plasmonic ring resonators with prior art. EO-modulators are expected to help replace electrical communication links with their optical counterparts for short-range applications. Potential candidates have to be compact (μm^2 footprint) to enable a dense co-integration of electronics and photonics. Furthermore, EO-modulators must be optimized for high speed (> 100GHz) and low insertion loss (<3 dB) to enable multi-gigabit operation. Extended Data Figure 6 shows the characteristics of state-of-the-art devices (photonic – crosses; plasmonic – circles) in terms of insertion loss and EO-bandwidth5,6,18,22,43,44,46–50. The different abbreviations represent various EO materials. Ideally, modulators should occupy the bluish area at the bottom right of the figure. However, large bandwidths correlate with large insertion loss. This is because the plasmonic waveguides also serve as highly conductive electrodes enabling a low RC-time constant, but, ohmic losses in the metals prevent low insertion losses. Contrarily, the resonant switching of photonic modulators enable low losses but suffer from limited bandwidths. Combining plasmonics and the resonant switching concept breaks the trade-off and enables high-speed and low losses modulators.

For the convenience of the reader, we provide a detailed summary of key metrics in Extended Data Table 3 (demonstrated plasmonic modulators) and in Extended Data Table 4 (photonic EO-modulators). The performance of the plasmonic ring resonator (last column) serves as reference in both tables. Extended Data Table 3 shows four non-resonant modulators based on various nonlinear effects and material systems such as $\chi^{(2)}$ in OEO-materials, free-carrier-dispersion (FCD) in silicon, FCD in transparent conductive oxides (TCO) and $\chi^{(2)}$ in barium titanate (BTO).

- The resonant approach (last column) outperforms its direct non-resonant counterpart (first column).
- Plasmonic resonators requires moderate driving voltages. And only the TCO based modulator is driven with 1V$_{\text{peak}}$. However, different data rates of 72 Gbit/s to 2.5 Gbit/s make a comparison challenging.
- Finally, we would like to note that applying the resonant plasmonic approach to other material systems would enable a further boost in performance for each individual technology. For instance, one can imagine TCO-based plasmonic resonators operating with ~mV driving voltages.

Extended Data Table 4 shows 6 photonic modulators based on FCD in silicon18,46, Franz-Keldysh Effect (FKE) in SiGe48, $\chi^{(2)}$ in barium titanate (BTO)47, $\chi^{(2)}$ in lithium niobate (LiNbO$_3$)50 and Pauli blocking in Graphene51.

Data availability statement

The data that support the findings of this study are available form the corresponding author upon reasonable request.

Extended Data

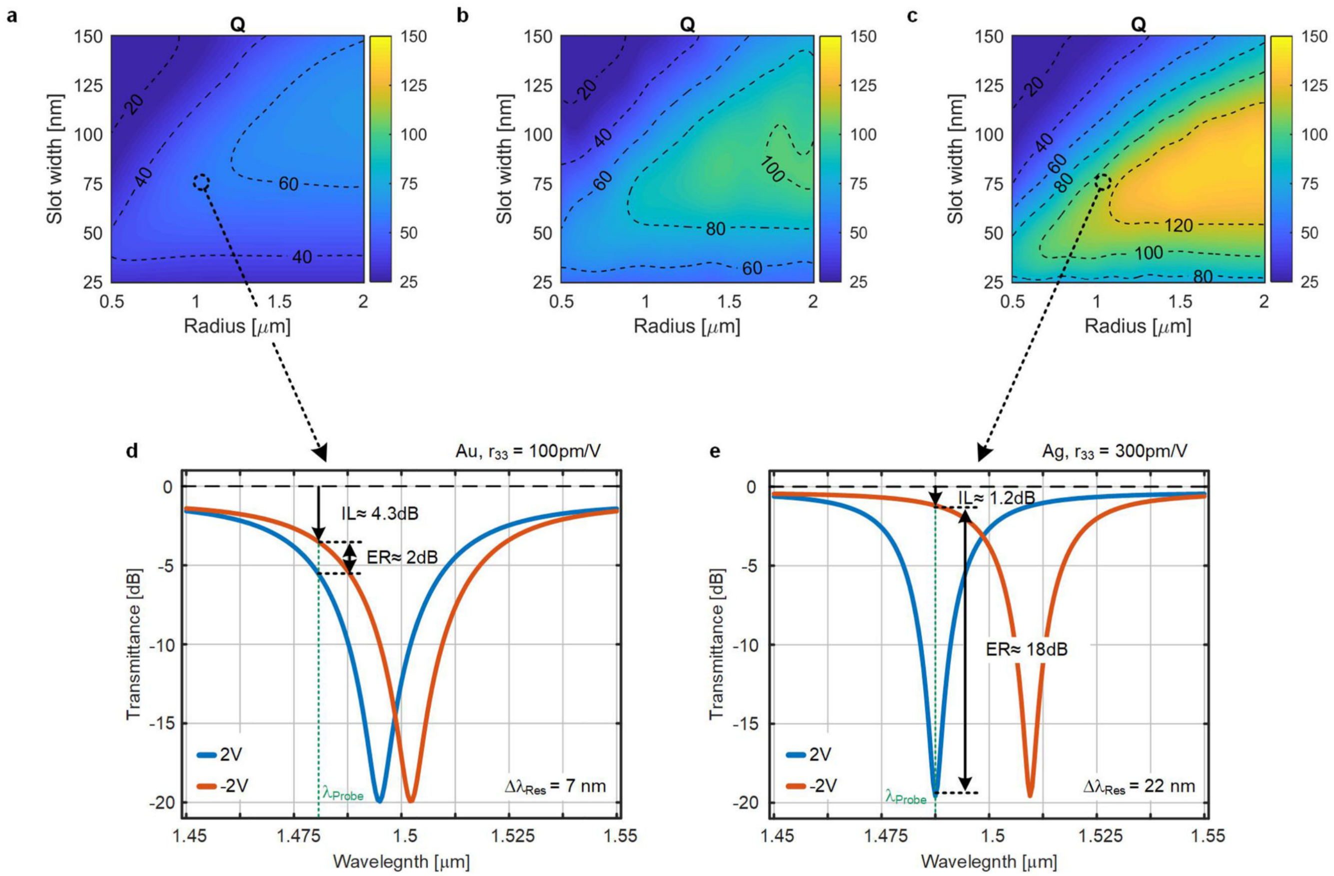

Extended Data Figure 1.

Resonator performance for various plasmonic materials. (a) Gold (Au) which is interesting for research due to its chemical stability. (b) Copper (Cu) is of interest as it is a CMOS-compatible material. (c) Silver (Ag) feature the best plasmonic properties and could be of interest for high performance applications. Switching capability of an (d) gold and (e) silver ring resonator for a 2V bias The latter utilizes the newest OEO material, which has a three-times-larger electro-optic coefficient r_{33}. The performance improvement enables a significant reduction in terms of the driving voltage. The number at the bottom right indicates the shift in the resonance wavelength.

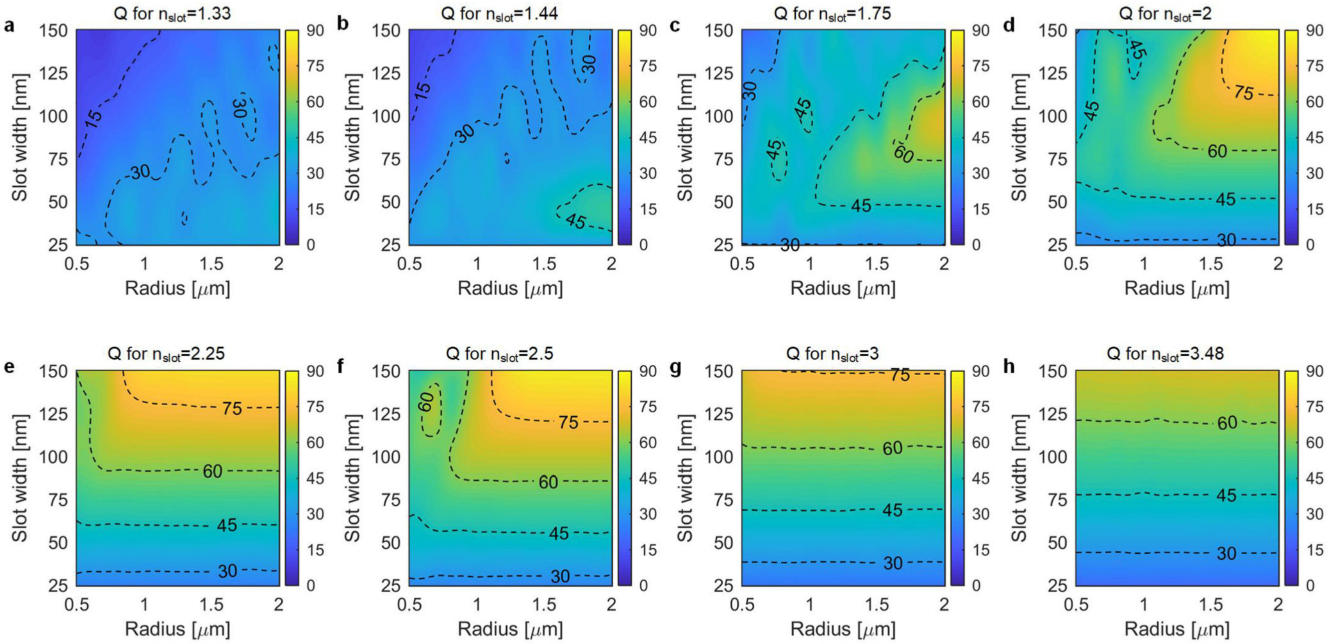

Extended Data Figure 2.

Q-factors of various materials filling the slot. The materials differ in their refractive index and one can observe that low n-materials are limited by bending loss (diagonal lines) while high n-materials are limited by propagation loss (parallel lines). Please note these simulations were performed with 150 nm height of the outer and inner electrode to account for limitations in fabrication processes different to ours.

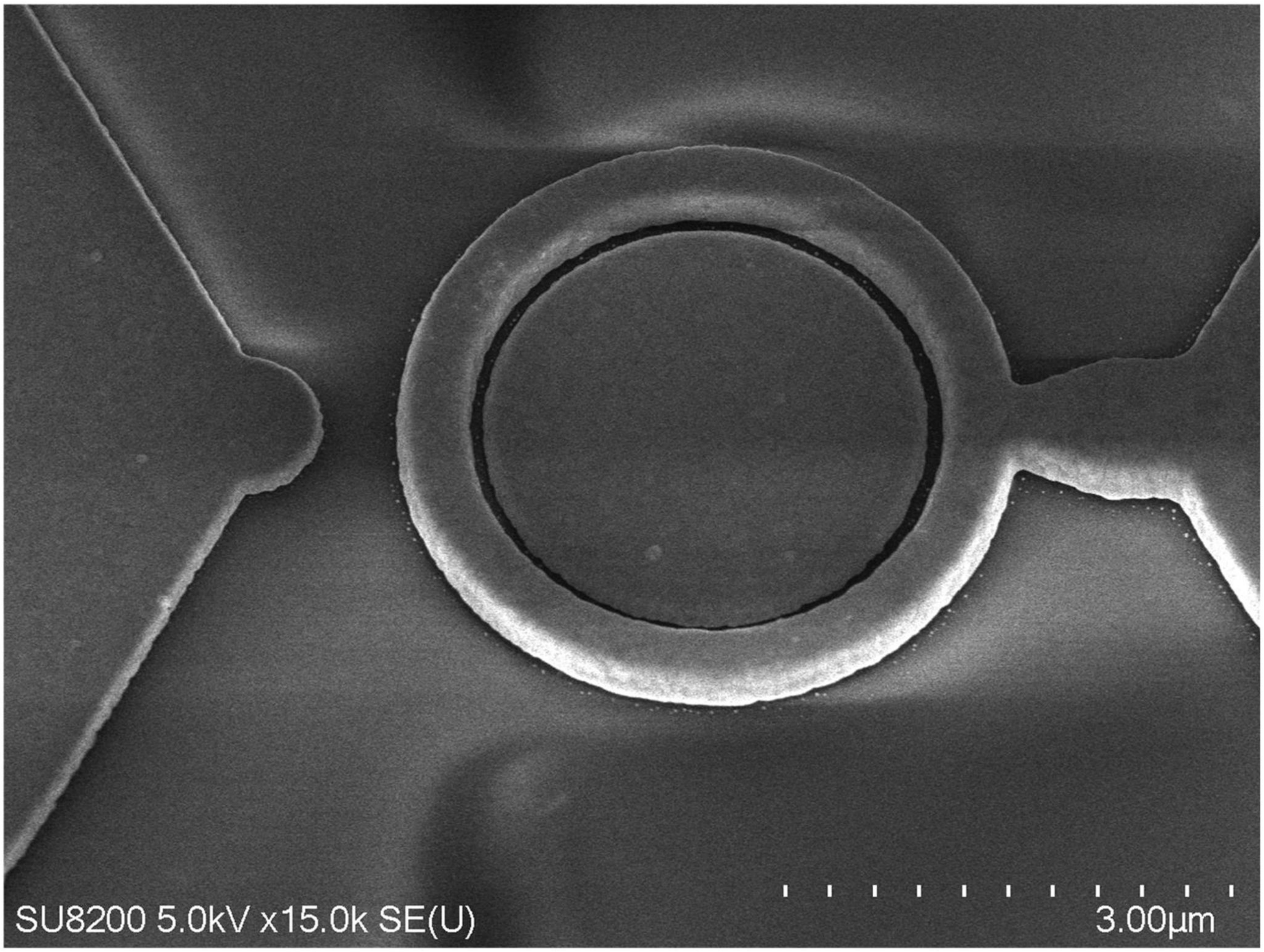

Extended Data Figure 3.

Tilted SEM image of a processed ring resonator. The different height of the outer and inner electrodes reduces the bending losses.

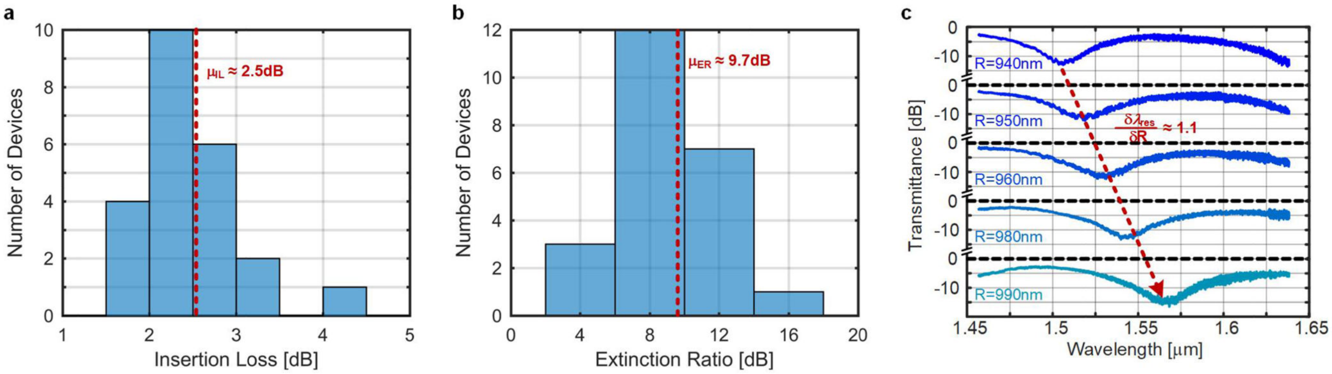

Extended Data Figure 4.

Reproducibility of plasmonic ring resonators. Insertion loss (a) and extinction ratio (b) histograms. Data are obtained from passive measurements of 23 devices with a designed slot with of 80 nm and radii ranging from 900 nm to 1100 nm. (c) Dependence of the resonance wavelength versus ring radius.

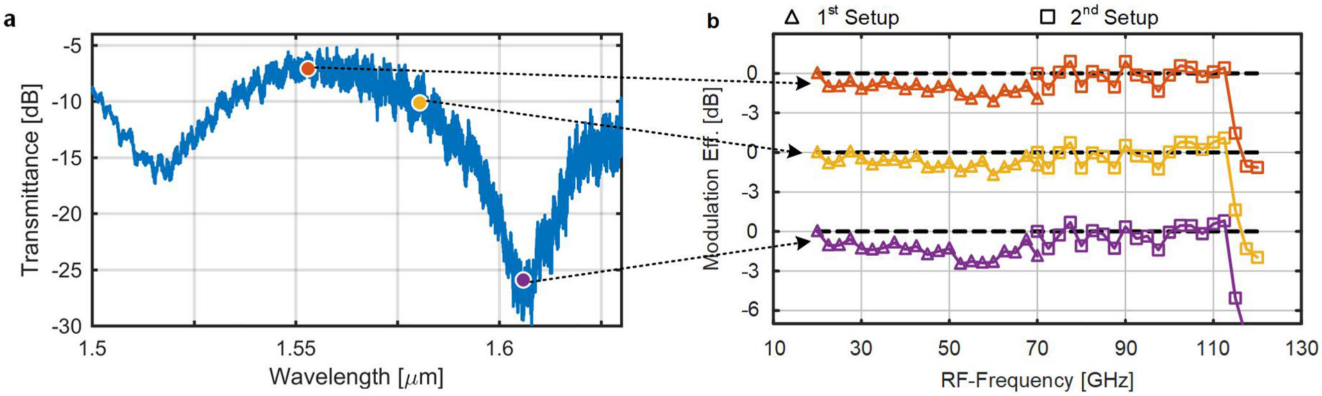

Extended Data Figure 5.

Transmission spectrum (a) and the measured bandwidth (b) at the off-resonance, 3dB and on-resonance operating point. No bandwidth limitation can be observed up to 110 GHz. The drop at 115 Ghz frequencies is due to a limited measurement setup. Recent studies show that the modulation efficiency at lower RF-frequency is not limited[44]

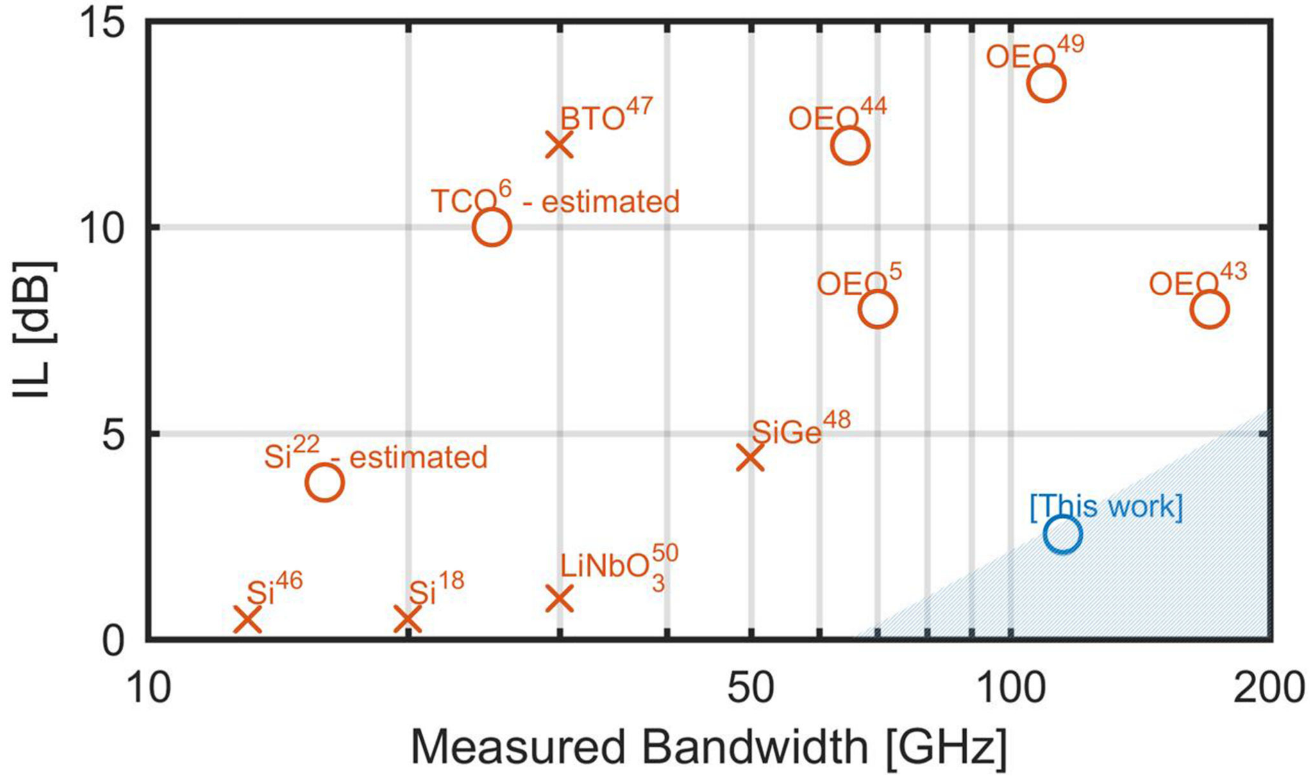

Extended Data Figure 6.

Technology overview in terms of insertion loss and bandwidth of electro-optic modulators. Ideal Candidates should feature low insertion loss with high electro-optic (EO) bandwidths found.

Extended Data Table 1

Measured DC-Sensitivity. The values of the radius and the slot width are the design parameters.

Radius [nm]/Slot width [nm], (Device Id)	*IL* [dB]	*ER* [dB]	$\Delta\lambda_{res}$/Bias [nm/V]
1200/80, (22)	~3	7	3
1260/80, (28)	~3	8	N.A.
1220/100, (36)	~2	8	1.8
1250/100, (39)	~2	6	2.1
1280/100, (42)	~2.5	7.5	2.33
1080/80, (79)	~2.75	10	2.75

Extended Data Table 2

Overview of the results obtained from data experiments with various devices

Radius [nm]/Slot width [nm], Device Id	**V_{peak} [V]**	**Data rate *(R)* [Gbit/s]**	**Bit-error-ratio *(BER)***	**$P_{opitcal}$[dBm]**
1230/80, (25)	~3.3	18	~$9x10^{-6}$	0
1250/80, (27)	~3.3	18	<$1x10^{-6}$	0
1200/100, (34)	~3.3	18	<$1x10^{-6}$	0
“	~3.3	36	~$2x10^{-5}$	4
“	~3.3	72	~$1x10^{-3}$	4
960/80, (88)	~5	72	~$2x10^{-3}$	6
“	~7.8	72	~$8x10^{-4}$	6
940/80, (86)	~7.8	72	~$4x10^{-4}$	12
930/80, (85)	~7.8	72	~$1x10^{-3}$	12

Extended Data Table 3

Comparison State-of-the art Plasmonic EO Modulator -*estimated values.

Reference	**43**	**22**	**6**	**38**	**this work**
Modulation Mech.	$\chi^{(2)}$ *OEO*	*FCD Si*	*FCD TCO*	$\chi^{(2)}$ *BTO*	$\chi^{(2)}$ *OEO*
IL [dB]	*~8*	*~3.8*	*~10*	*25*	*~2.5*
Fiber-2-fiber loss[dB]	*34*	*N.A.*	*N.A.*	*N.A.*	*16*
ER [dB]	*N.A.*	*6-10*	*6*	*>15*	*10*
L_{Active} [μm]	*20*	*1*	*4*	*10*	*6*
Bandwidth [GHz]	*>170*	*16°*	*>2.5*	*N.A.*	*>110*
Data Rate [Gbit/s]	*100*	*<<1*	*2.5*	*72*	*72*
BER					
Driving Voltage [V_{peak}]	*4*	*6*	*1*	*2.8*	*3.3*
Energy Consumption [fJ/Bit]	*48°*	*~100*	*N.A.*	*N.A.*	*12*

Extended Data Table 4

Comparison State-of-the art Photonic EO – Modulator

Reference	**18**	**46**	**47**	**50**	**51**	**48**	**this work**
Modulation Mech.	*FCD Si*	*FCD Si*	$\chi^{(2)}$*BTO*	$\chi^{(2)}$*LiNbO*$_3$	*Pauli Blocking Graphene*	*FKE Si Ge*	$\chi^{(2)}$*OEO*
IL [dB]	~0.5	~0.5	>12	1	N.A.	4.4	~2.5
ER [dB]	12	10	N.A.	~7*	30	4.2	10
L_{active} [μm]	15	30	37	~600*	~250	40	6
Bandwidth [GHz]	~17	13	30*	30	30	>50	>110

Reference	**18**	**46**	**47**	**50**	**51**	**48**	**this work**
Data Rate [Gbit/s]	44	12	N.A.	40	22	50	72
Driving Voltage [V_{peak}]	0.5	2.46	16	2.88	3.75	1	3.3
Energy Consumption [fJ/Bit]	<1	N.A.	N.A.	240	800	13.8	12
Q	6000	15000	N.A.	8000	<1200	N.A	50
Temp. Stability [$\Delta\lambda_{res}$ K^{-1} $FWHM^{-1}$]	100%	N.A.	N.A.	N.A.	N.A.	N.A.	0.4%
Sensitivity [$\Delta\lambda_{res}$ V^{-1} $FWHM^{-1}$]	100%	11%	N.A.	N.A.	N.A.	N.A.	5%

Supplementary Material

Refer to Web version on PubMed Central for supplementary material.

Acknowledgment

The authors thank Ute Drechsler and Hans-Rudolf Benedickter for their technical assistance. Also we would like to acknowledge partial funding of this project by the EU Project PLASMOFAB (688166), by the ERC grant PLASILOR (640478), by the National Science Foundation (NSF) (DMR-1303080) and by the Air Force Office of Scientific Research grants (FA9550-15-1-0319 and FA9550-14-1-0138). N. K. acknowledges support from the Virginia Microelectronics Consortium and the Virginia Commonwealth University Presidential Research Quest Fund. This work was carried out at the BRNC Zurich and ETH Zurich.

References

1. Maier SA, et al. Plasmonics—A Route to Nanoscale Optical Devices. Advanced Materials. 2001; 13:1501–1505.
2. Gramotnev DK, Bozhevolnyi SI. Plasmonics beyond the diffraction limit. Nat Photonics. 2010; 4:83–91. DOI: 10.1038/nphoton.2009.282
3. Dionne JA, Diest K, Sweatlock LA, Atwater HA. PlasMOStor: A Metal–Oxide–Si Field Effect Plasmonic Modulator. Nano Letters. 2009; 9:897–902. DOI: 10.1021/nl803868k [PubMed: 19170558]
4. Sorger VJ, Lanzillotti-Kimura Norberto D, Ma R-M, Zhang X. Ultra-compact silicon nanophotonic modulator with broadband response. Nanophotonics. 2012; 1:17.doi: 10.1515/nanoph-2012-0009
5. Haffner C, et al. All-plasmonic Mach–Zehnder modulator enabling optical high-speed communication at the microscale. Nat Photon. 2015; 9:525–528.
6. Keeler, GA., et al. Th3I.1. Optical Fiber Communication Conference; Optical Society of America; 2017.
7. Min B, et al. High-Q surface-plasmon-polariton whispering-gallery microcavity. Nature. 2009; 457:455–458. [PubMed: 19158793]
8. Brolo AG. Plasmonics for future biosensors. Nat Photon. 2012; 6:709–713.
9. Cai W, Vasudev AP, Brongersma ML. Electrically Controlled Nonlinear Generation of Light with Plasmonics. Science. 2011; 333:1720–1723. DOI: 10.1126/science.1207858 [PubMed: 21940887]
10. Kauranen M, Zayats AV. Nonlinear plasmonics. Nat Photon. 2012; 6:737–748.
11. Ndukaife JC, et al. Long-range and rapid transport of individual nano-objects by a hybrid electrothermoplasmonic nanotweezer. Nat Nano. 2016; 11:53–59. DOI: 10.1038/nnano.2015.248
12. Hirsch LR, et al. Nanoshell-mediated near-infrared thermal therapy of tumors under magnetic resonance guidance. Proceedings of the National Academy of Sciences. 2003; 100:13549–13554. DOI: 10.1073/pnas.2232479100
13. Khurgin JB. How to deal with the loss in plasmonics and metamaterials. Nat Nano. 2015; 10:2–6. DOI: 10.1038/nnano.2014.310

14. Miller DAB. Attojoule Optoelectronics for Low-Energy Information Processing and Communications; a Tutorial Review. J Lightwave Technol. 2017; :1–1. DOI: 10.1109/JLT.2017.2647779

15. Reed GT, Mashanovich G, Gardes FY, Thomson DJ. Silicon optical modulators. Nat Photon. 2010; 4:518–526.

16. Vahala KJ. Optical microcavities. Nature. 2003; 424:839–846. [PubMed: 12917698]

17. Xu Q, Schmidt B, Pradhan S, Lipson M. Micrometre-scale silicon electro-optic modulator. Nature. 2005; 435:325–327. [PubMed: 15902253]

18. Timurdogan E, et al. An ultralow power athermal silicon modulator. Nat Commun. 2014; 5doi: 10.1038/ncomms5008

19. Sun C, et al. Single-chip microprocessor that communicates directly using light. Nature. 2015; 528:534–538. DOI: 10.1038/nature16454 [PubMed: 26701054]

20. Emboras A, et al. Atomic Scale Plasmonic Switch. Nano Letters. 2015; doi: 10.1021/acs.nanolett.5b04537

21. Oulton RF, Sorger VJ, Genov DA, Pile DFP, Zhang X. A hybrid plasmonic waveguide for subwavelength confinement and long-range propagation. Nat Photon. 2008; 2:496–500.

22. Zhu S, Lo GQ, Kwong DL. Phase modulation in horizontal metal-insulator-silicon-insulator-metal plasmonic waveguides. Opt Express. 2013; 21:8320–8330. DOI: 10.1364/OE.21.008320 [PubMed: 23571922]

23. Hill MT, et al. Lasing in metallic-coated nanocavities. Nat Photon. 2007; 1:589–594.

24. Bozhevolnyi SI, Volkov VS, Devaux E, Laluet J-Y, Ebbesen TW. Channel plasmon subwavelength waveguide components including interferometers and ring resonators. Nature. 2006; 440:508–511. [PubMed: 16554814]

25. Kress SJP, et al. A customizable class of colloidal-quantum-dot spasers and plasmonic amplifiers. Science Advances. 2017; 3doi: 10.1126/sciadv.1700688

26. Zhu W, et al. Surface plasmon polariton laser based on a metallic trench Fabry-Perot resonator. Science Advances. 2017; 3doi: 10.1126/sciadv.1700909

27. Sun, SS., Dalton, LR. Introduction to Organic Electronic and Optoelectronic Materials and Devices. Taylor & Francis; 2008.

28. Zanotto S, Morichetti F, Melloni A. Fundamental limits on the losses of phase and amplitude optical actuators. Laser & Photonics Reviews. 2015; 9:666–673.

29. Delacour C, et al. Efficient Directional Coupling between Silicon and Copper Plasmonic Nanoslot Waveguides: toward Metal–Oxide–Silicon Nanophotonics. Nano Letters. 2010; 10:2922–2926. DOI: 10.1021/nl101065q [PubMed: 20698605]

30. Bogaerts W, et al. Silicon microring resonators. Laser & Photonics Reviews. 2012; 6:47–73.

31. Becker J, Trügler A, Jakab A, Hohenester U, Sönnichsen C. The Optimal Aspect Ratio of Gold Nanorods for Plasmonic Bio-sensing. Plasmonics. 2010; 5:161–167. DOI: 10.1007/s11468-010-9130-2

32. Chang F, Onohara K, Mizuochi T. Forward error correction for 100 G transport networks. IEEE Communications Magazine. 2010; 48

33. Haffner C, et al. Harnessing nonlinearities near material absorption resonances for reducing losses in plasmonic modulators. Optical Materials Express. 2017; 7:2168–2181. DOI: 10.1364/OME.7.002168

34. Jin W, et al. Benzocyclobutene barrier layer for suppressing conductance in nonlinear optical devices during electric field poling. Applied Physics Letters. 2014; 104:243304.doi: 10.1063/1.4884829

35. Heni W, et al. Nonlinearities of organic electro-optic materials in nanoscale slots and implications for the optimum modulator design. Opt Express. 2017; 25:2627–2653. DOI: 10.1364/OE.25.002627 [PubMed: 29519106]

36. Kieninger, C., et al. STu3N.2. Conference on Lasers and Electro-Optics; Optical Society of America;

37. Maier, SA. Plasmonics: Fundamentals and Applications. Springer; US: 2007.

38. Messner, A., et al. Th5C.7. Optical Fiber Communication Conference Postdeadline Papers; Optical Society of America;

39. Watanabe T, Ayata M, Koch U, Fedoryshyn Y, Leuthold J. Perpendicular Grating Coupler Based on a Blazed Anti-Back-Reflection Structure. J Lightwave Technol. 2017

40. Kretz J, Dreeskornfeld L, Ilicali G, Lutz T, Weber W. Comparative study of calixarene and HSQ resist systems for the fabrication of sub-20nm MOSFET device demonstrators. Microelectronic Engineering. 2005; 78–79:479–483. DOI: 10.1016/j.mee.2004.12.061

41. Elder DL, et al. Effect of Rigid Bridge-Protection Units, Quadrupolar Interactions, and Blending in Organic Electro-Optic Chromophores. Chemistry of Materials. 2017; doi: 10.1021/acs.chemmater.7b02020

42. Gheorma IL, Osgood RM. Fundamental limitations of optical resonator based high-speed EO modulators. IEEE Photonics Technology Letters. 2002; 14:795–797. DOI: 10.1109/LPT.2002.1003096

43. Hoessbacher C, et al. Plasmonic modulator with 170 GHz bandwidth demonstrated at 100 GBd NRZ. Opt Express. 2017; 25:1762–1768. DOI: 10.1364/OE.25.001762 [PubMed: 29519029]

44. Melikyan A, et al. High-speed plasmonic phase modulators. Nat Photon. 2014; 8:229–233.

45. Josten A, et al. Modified Godard Timing Recovery for Non Integer Oversampling Receivers. Applied Sciences. 2017; 7:655.

46. Alloatti L, Cheian D, Ram RJ. High-speed modulator with interleaved junctions in zero-change CMOS photonics. Applied Physics Letters. 2016; 108:131101.

47. Girouard P, et al. chi2 Modulator With 40-GHz Modulation Utilizing BaTiO3 Photonic Crystal Waveguides. IEEE Journal of Quantum Electronics. 2017; 53:1–10.

48. Srinivasan, A., et al. Tu3D.7. Optical Fiber Communication Conference; Optical Society of America;

49. Haffner C, et al. Plasmonic Organic Hybrid Modulators: Scaling Highest Speed Photonics to the Microscale. Proceedings of the IEEE. 2016; 104:2362–2379. DOI: 10.1109/JPROC.2016.2547990

50. Wang C, Zhang M, Stern B, Lipson M, Loncar M. Nanophotonic lithium niobate electro-optic modulators. arXiv. 2017 preprint arXiv:1701.06470.

51. Phare CT, Daniel Lee Y-H, Cardenas J, Lipson M. Graphene electro-optic modulator with 30 GHz bandwidth. Nat Photon. 9:511–514. DOI: 10.1038/nphoton.2015.122

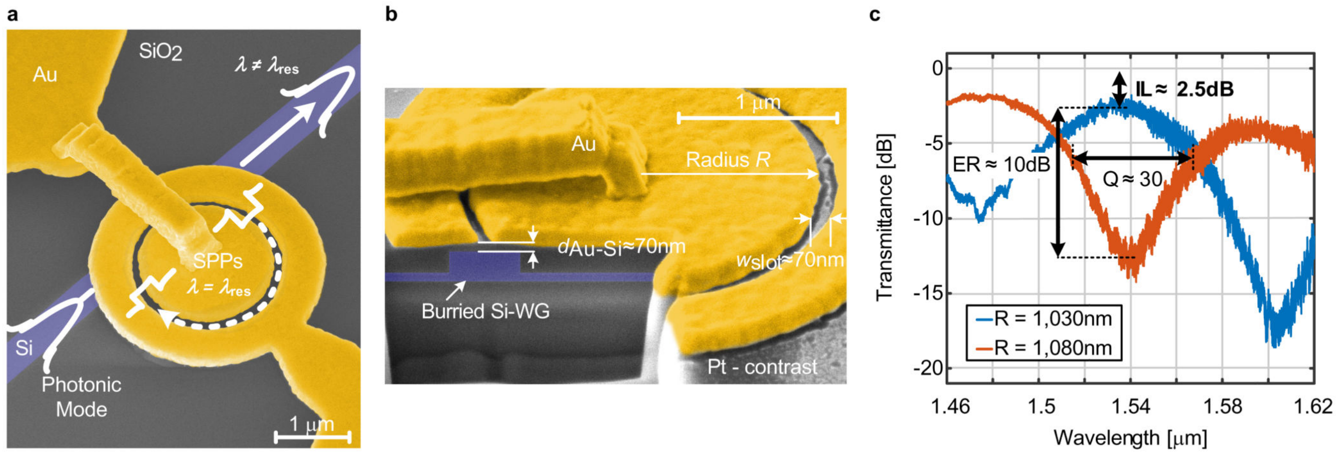

Figure 1.

False-colored SEM image of a plasmonic ring resonator and the corresponding transmittance over wavelength. (a) Top view and (b) cross section of the resonator. Photonic modes propagating in the buried silicon waveguide resonator couple partially to the SPPs in the metal-insulator-metal-ring when the resonance condition is fulfilled. While out of resonance operation results in a low loss light transmission. (c) Passive measurements of two identical ring resonators that only differ in radii (blue - 1030 nm; red - 1080 nm). Due to the resonant approach, insertion losses of 2.5 dB are measured with extinction ratios (ER) above 10 dB.

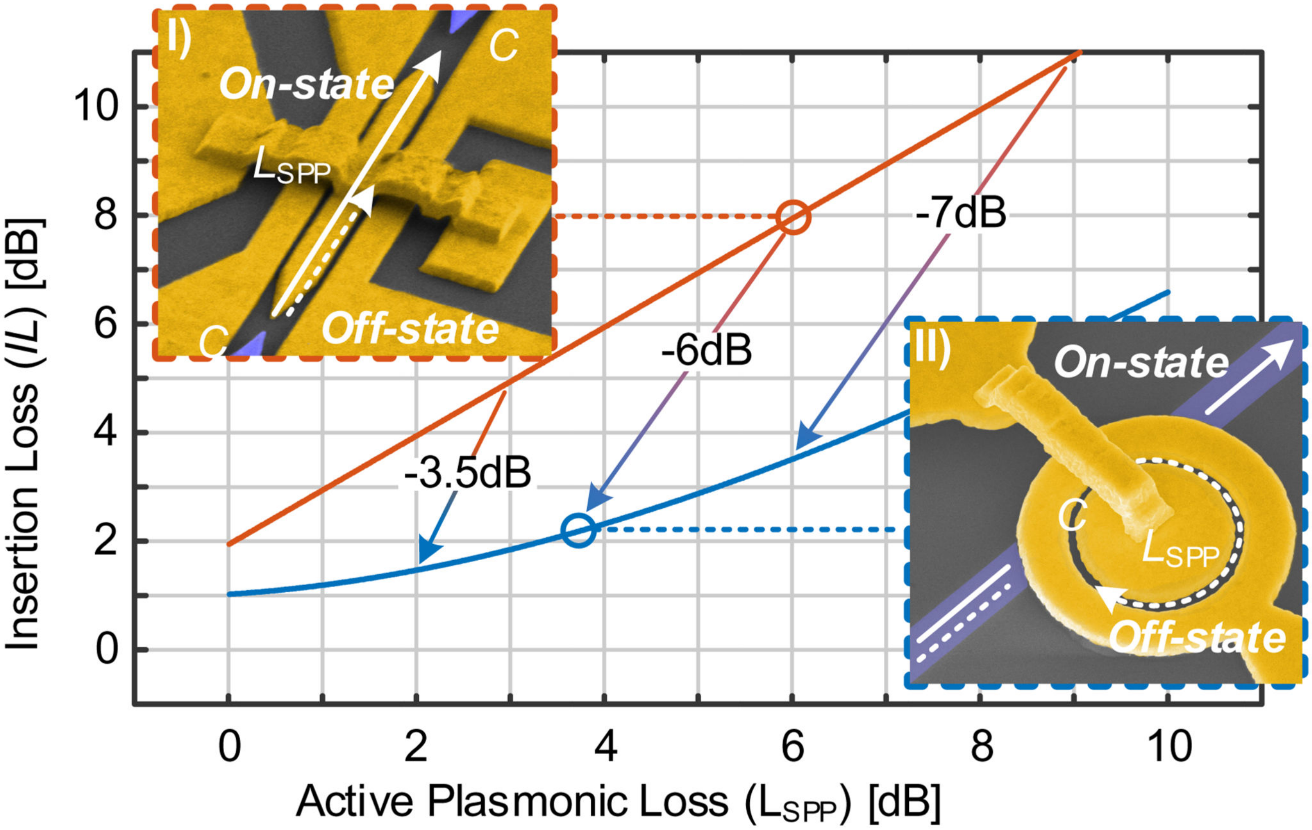

Figure 2.

Theoretical loss advantage of critical coupled resonant over non-resonant push-pull Mach-Zehnder devices. The IL are plotted over the active plasmonic loss (L_{SPP}) in the slot waveguide of the MZ (left inset, red) and resonator (right inset, blue). Losses can be reduced by more than 6 dB. This is due to following reasons: I) bypassing mechanism – only a fraction of light experiences plasmonic losses; II) resonant enhancement – resonators achieve the same modulation depth for shorter devices than their non-resonant counterpart (indicated by the arrows); and III) coupling scheme – non-resonant approaches require two photonic/SPP converters while resonant approaches require only one.

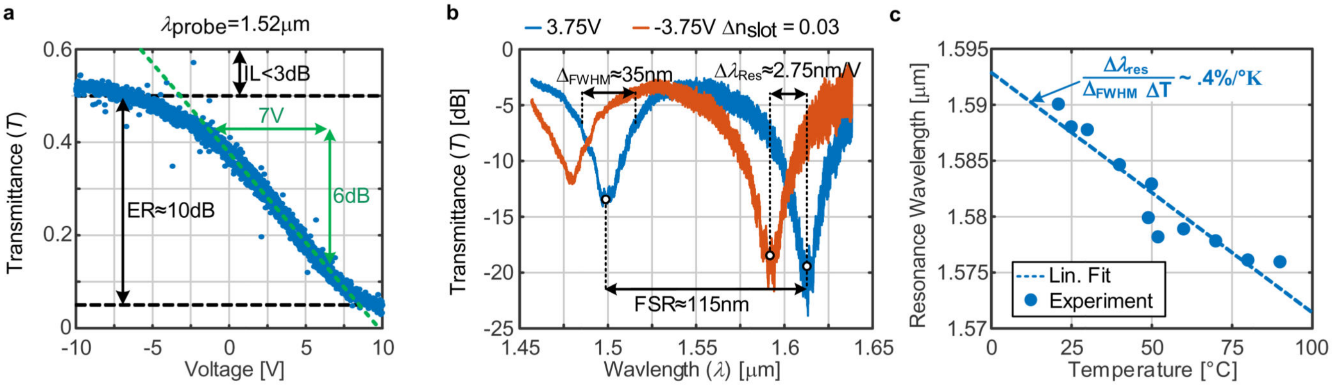

Figure 3.

Sensitivity and stability of the plasmonic resonator. (a) Voltage sensitivity of the resonator's transmittance. (b) Sensitivity of the ring as a function of the wavelength. A change (Δn_{slot}≈0.03) in the refractive index of the slot-filling material causes a large change of the resonance wavelength (blue/red). (c) The resonator shows stable operation across a large thermal variation. These characteristics make the plasmonic MIM-ring resonator a promising candidate in the field of optical modulators and sensors.

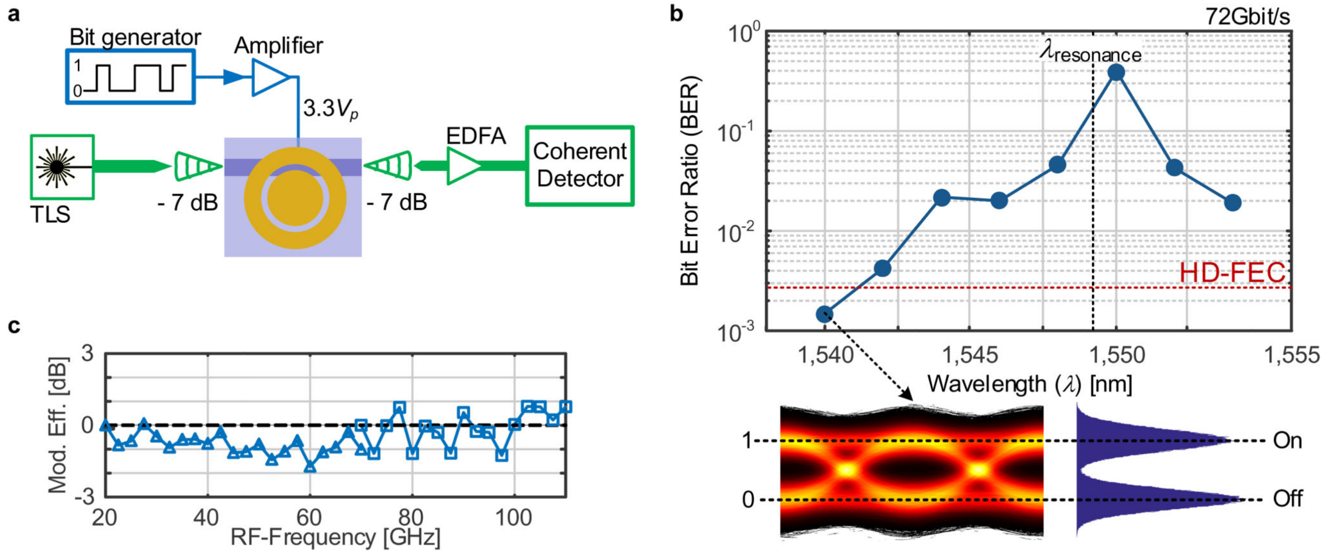

Figure 4.

High-speed data experiments with a plasmonic ring resonator used as an EO-modulator. (a) Depicts the experimental setup. (b) Bit-error-ratio (BER) vs. wavelength for a resonator with $\lambda_{resonance}$ = 1549nm. BERs below the hard-decision forward error correction (HD-FEC) limit show successful data modulation and detection without the use of a temperature control. The BER increases at the resonance wavelength as expected from the notch-filter response of the resonator. (c) Shows the bandwidth of the plasmonic resonator in the bottom, which is beyond 110 GHz.